the formation of the solar system and was incorporated into planetesimal bodies. Consequently, if the formation of the solar nebula was typical, our work implies that interstellar ices from the parent molecular cloud core—including the most fundamental life-fostering ingredient, water—are widely available to all young planetary systems.

REFERENCES AND NOTES

1. T. Encrenaz, *Annu. Rev. Astron. Astrophys.* **46**, 57–87 (2008).
2. D. J. Lawrence *et al.*, *Science* **339**, 292–296 (2013).
3. J. J. Barnes *et al.*, *Earth Planet. Sci. Lett.* **390**, 244–252 (2014).
4. T. Usui, C. M. O'D. Alexander, J. Wang, J. I. Simon, J. H. Jones, *Earth Planet. Sci. Lett.* **357-358**, 119–129 (2012).
5. F. Robert, D. Gautier, B. Dubrulle, *Space Sci. Rev.* **92**, 201–224 (2000).
6. C. Ceccarelli *et al.*, in *Protostars and Planets VI*, H. Beuther *et al.*, Eds. (Univ. of Arizona, Tucson, 2014), pp. 859–882.
7. E. F. van Dishoeck, E. A. Bergin, D. C. Lis, J. I. Lunine, in *Protostars and Planets VI*, H. Beuther *et al.*, Eds. (Univ. of Arizona, Tucson, 2014), pp. 835–858.
8. D. Bockelée-Morvan *et al.*, *Icarus* **133**, 147–162 (1998).
9. P. Eberhardt, M. Reber, D. Krankowsky, R. R. Hodges, *Astron. Astrophys.* **302**, 301 (1995).
10. C. M. O'D. Alexander *et al.*, *Science* **337**, 721–723 (2012).
11. E. Dartois *et al.*, *Astron. Astrophys.* **399**, 1009–1020 (2003).
12. A. Coutens *et al.*, *Astron. Astrophys.* **539**, A132 (2012).
13. M. V. Persson, J. K. Jørgensen, E. F. van Dishoeck, *Astron. Astrophys.* **541**, A39 (2012).
14. M. V. Persson, J. K. Jørgensen, E. F. van Dishoeck, D. Harsono, *Astron. Astrophys.* **563**, A74 (2014).
15. R. Visser, E. F. van Dishoeck, S. D. Doty, C. P. Dullemond, *Astron. Astrophys.* **495**, 881–897 (2009).
16. L. Yang, F. J. Ciesla, C. M. O'D. Alexander, *Icarus* **226**, 256–267 (2013).
17. Materials and methods are available as supplementary material on *Science* Online.
18. Y. Aikawa, E. Herbst, *Astrophys. J.* **526**, 314–326 (1999).
19. L. I. Cleeves, F. C. Adams, E. A. Bergin, *Astrophys. J.* **772**, 5 (2013).
20. E. Chapillon, B. Parise, S. Guilloteau, F. Du, *Astron. Astrophys.* **533**, A143 (2011).
21. T. Umebayashi, N. Katsuma, H. Nomura, *Astrophys. J.* **764**, 104 (2013).
22. T. Minamidani *et al.*, *Astron. J.* **141**, 73 (2011).
23. J. Geiss, G. Gloeckler, *Space Sci. Rev.* **106**, 3–18 (2003).
24. K. Willacy, P. M. Woods, *Astrophys. J.* **703**, 479–499 (2009).
25. T. Albertsson, D. Semenov, T. Henning, *Astrophys. J.* **784**, 39 (2014).
26. E. A. Bergin, W. D. Langer, P. F. Goldsmith, *Astrophys. J.* **441**, 222 (1995).
27. K. Furuya, Y. Aikawa, H. Nomura, F. Hersant, V. Wakelam, *Astrophys. J.* **779**, 11 (2013).
28. F. J. Ciesla, S. A. Sandford, *Science* **336**, 452–454 (2012).
29. F. J. Ciesla, *Astrophys. J.* **784**, L1 (2014).

ACKNOWLEDGMENTS

L.I.C. and E.A.B. acknowledge support by NSF grant AST-1008800. C.M.O'D.A. was partially supported by NASA Astrobiology grant NNA09DA81A and by NASA Cosmochemistry grant NNX11AG67G. F.D. was supported by NASA grant NNX12A193G. T.J.H. was supported by U.K. Science and Technology Facilities Council grant ST/J001627/1.

SUPPLEMENTARY MATERIALS

www.sciencemag.org/content/345/6204/1590/suppl/DC1
Materials and Methods
Figs. S1 to S4
Tables S1 to S4
References (*30*–*71*)

30 June 2014; accepted 21 August 2014
10.1126/science.1258066

WATER SPLITTING

Water photolysis at 12.3% efficiency via perovskite photovoltaics and Earth-abundant catalysts

Jingshan Luo,[1,2] Jeong-Hyeok Im,[1,3] Matthew T. Mayer,[1] Marcel Schreier,[1] Mohammad Khaja Nazeeruddin,[1] Nam-Gyu Park,[3] S. David Tilley,[1] Hong Jin Fan,[2] Michael Grätzel[1]*

Although sunlight-driven water splitting is a promising route to sustainable hydrogen fuel production, widespread implementation is hampered by the expense of the necessary photovoltaic and photoelectrochemical apparatus. Here, we describe a highly efficient and low-cost water-splitting cell combining a state-of-the-art solution-processed perovskite tandem solar cell and a bifunctional Earth-abundant catalyst. The catalyst electrode, a NiFe layered double hydroxide, exhibits high activity toward both the oxygen and hydrogen evolution reactions in alkaline electrolyte. The combination of the two yields a water-splitting photocurrent density of around 10 milliamperes per square centimeter, corresponding to a solar-to-hydrogen efficiency of 12.3%. Currently, the perovskite instability limits the cell lifetime.

Compared with other energy resources, solar energy is sustainable and far more abundant than our projected energy needs as a species; thus, it is considered as the most promising energy source for the future. Because of the diffuse nature of solar energy, large arrays of solar cells will have to be implemented. Currently, electricity produced by silicon (Si) solar cells is too costly to achieve grid parity. In contrast, the dye-sensitized solar cell (DSSC) (*1*, *2*) uses cheap materials and facile solution processes. A related type of low-cost solution-processed solar cell based on a perovskite formulation has recently emerged (*3*–*10*). The rapid rise of the solar-to-electric power conversion efficiency (currently 17.9% certified) in less than 5 years makes it highly promising for large-scale commercialization (*11*). Long-term stability, however, is currently a challenge with these solar cells.

The conversion of solar energy directly into fuels is a promising solution to the challenge of intermittency in renewable energy sources, addressing the issues of effective storage and transport. In nature, plants harvest solar energy and convert it into chemical fuel via photosynthesis. Inspired by nature, artificial photosynthesis has been proposed as a viable way to store the solar energy as fuel (*12*, *13*). Hydrogen, which is the simplest form of energy carrier, can be generated renewably with solar energy through photoelectrochemical water splitting or by photovoltaic (PV)–driven electrolysis. Intensive research has been conducted in the past several decades to develop efficient photoelectrodes, catalysts, and device architectures for solar hydrogen generation (*14*–*20*). However, it still remains a great challenge to develop solar water-splitting systems that are both low-cost and efficient enough to generate fuel at a price that is competitive with fossil fuels (*21*).

Splitting water requires an applied voltage of at least 1.23 V to provide the thermodynamic driving

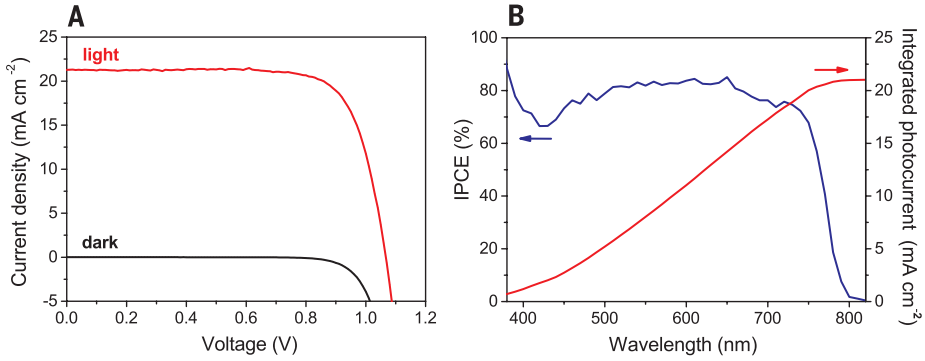

Fig. 1. Performance of perovskite solar cell. (**A**) Current density–potential curve (*J*–*V*) of the perovskite solar cell under dark and simulated AM 1.5G 100 mW cm^{-2} illumination. (**B**) IPCE spectrum of the perovskite solar cell and the integrated photocurrent with the AM 1.5G solar spectrum.

[1]Laboratory of Photonics and Interfaces, Institute of Chemical Sciences and Engineering, School of Basic Sciences, Ecole Polytechnique Fédérale de Lausanne (EPFL), CH-1015 Lausanne, Switzerland. [2]Division of Physics and Applied Physics, School of Physical and Mathematical Sciences, Nanyang Technological University (NTU), 637371 Singapore. [3]School of Chemical Engineering and Department of Energy Science, Sungkyunkwan University (SKKU), Suwon 440-746, Korea.
***Corresponding author. E-mail: michael.graetzel@epfl.ch**

force. Because of the practical overpotentials associated with the reaction kinetics, a substantially larger voltage is generally required, and commercial electrolysers typically operate at a voltage of 1.8 to 2.0 V (*22*). This complicates PV-driven electrolysis using conventional solar cells—such as Si, thin-film copper indium gallium selenide (CIGS), and cadmium telluride (CdTe)—because of their incompatibly low open-circuit voltages. To drive electrolysis with these conventional devices, three to four cells must be connected in series or a DC–DC power converter must be used in order to achieve reasonable efficiency. Multijunction solar cells—such as triple-junction silicon (*18*, *23*), III-V–based solar cells (*16*), and most recently CIGS solar cells in tandem—have also been applied to water splitting (*24*). In contrast, perovskite solar cells have achieved open-circuit voltages of at least 0.9 V and up to 1.5 V according to recent reports (*25*–*27*), which is sufficient for efficient water splitting by connecting just two in series.

Here, we present our results on water splitting using state-of-the-art perovskite solar cells. Our cell was based on $CH_3NH_3PbI_3$, which is processed by means of a two-step spin coating method at 100°C (*28*). The current density–voltage (*J*–*V*) characteristic of a representative perovskite solar cell is shown in Fig. 1A under simulated AM 1.5G solar irradiation (100 mW cm^{-2}) and in the dark. The cell has a short-circuit photocurrent density, open-circuit voltage, and fill factor of 21.3 mA cm^{-2}, 1.06 V, and 0.76, respectively, yielding a solar-to-electric power conversion efficiency (PCE) of 17.3%. The incident photon-to-current conversion efficiency (IPCE) (Fig. 1B) shows that the perovskite solar cell is active from the ultraviolet to 800 nm, which is in good agreement with the band gap (1.5 eV). An integration of the IPCE spectrum with the AM 1.5G solar photon flux yields a current density of 21.1 mA cm^{-2}, corroborating the value that we obtained from the *J*–*V* measurements.

With the highly efficient perovskite solar cell in hand, the next step was to overcome the large water-splitting overpotentials that are typically required to generate H_2 and O_2 at a practical rate. For this purpose, efficient electrocatalysts must be implemented. Our intention was to avoid using the conventional expensive noble metals of low abundance, such as Pt, RuO_2, and IrO_2. In the past decades, tremendous efforts have been devoted to developing low-cost and high-efficiency electrocatalysts for water splitting—for example, MoS_2 and NiMo for the H_2 evolution reaction (HER) (*29*–*31*), and cobalt-phosphate, metal oxides, and hydroxides for the O_2 evolution reaction (OER) (*17*, *32*–*34*). For sustained overall water splitting, the catalysts for the HER and OER must be operated in the same electrolyte. Furthermore, in order to minimize overpotentials in the electrolyte, water splitting should be carried out in either strongly acidic or alkaline electrolyte (*35*). This requirement is a challenge for most of the Earth-abundant catalysts because a highly active catalyst in acidic electrolyte may not be active or even stable in basic electrolyte. For example, MoS_2 is highly active for the HER in acidic electrolyte (*36*), but it is unstable in base. Similarly, most of the metal oxides and hydroxides for the OER are not stable in acidic electrolyte. Thus, it is crucial to develop a bifunctional catalyst that has high activity toward both the HER and OER in the same electrolyte (either strongly acidic or strongly basic). Moreover, the use of a bifunctional catalyst simplifies the system, lowering the manufacturing cost and thus the cost of the resulting hydrogen.

Nickel (Ni) foam is used as the electrode for commercial alkaline electrolysers because of its Earth abundance and porous three-dimensional structure (*22*). Recently, $Ni(OH)_2$ has received great attention for the OER (*33*, *37*, *38*), and it has been shown that the activity could be improved by the incorporation of iron (*39*–*41*). Furthermore, the $Ni(OH)_2$ modified nickel surface has shown an HER rate around four times higher than bare nickel in alkaline electrolyte (*42*, *43*). The high performance of $Ni(OH)_2$ toward both the OER and HER in strongly basic solutions makes it an exceptional bifunctional catalyst. Here, we incorporated iron (Fe) into $Ni(OH)_2$ to form NiFe layered double hydroxides (LDHs), which were directly grown on the surface of the Ni foam by means of a simple one-step hydrothermal growth method (*28*, *40*). For comparison, pristine Ni foam, $Ni(OH)_2$ on Ni foam, and Ni foam with ~3.5-nm Pt nanoparticles (deposited by sputtering on both sides of the foam) electrodes were also studied. The OER characteristics of these different electrodes in 1 M NaOH are shown in Fig. 2A at a scan rate of 1 mV s^{-1}, with the scan direction from positive to negative on the reversible hydrogen electrode (RHE) scale (currents

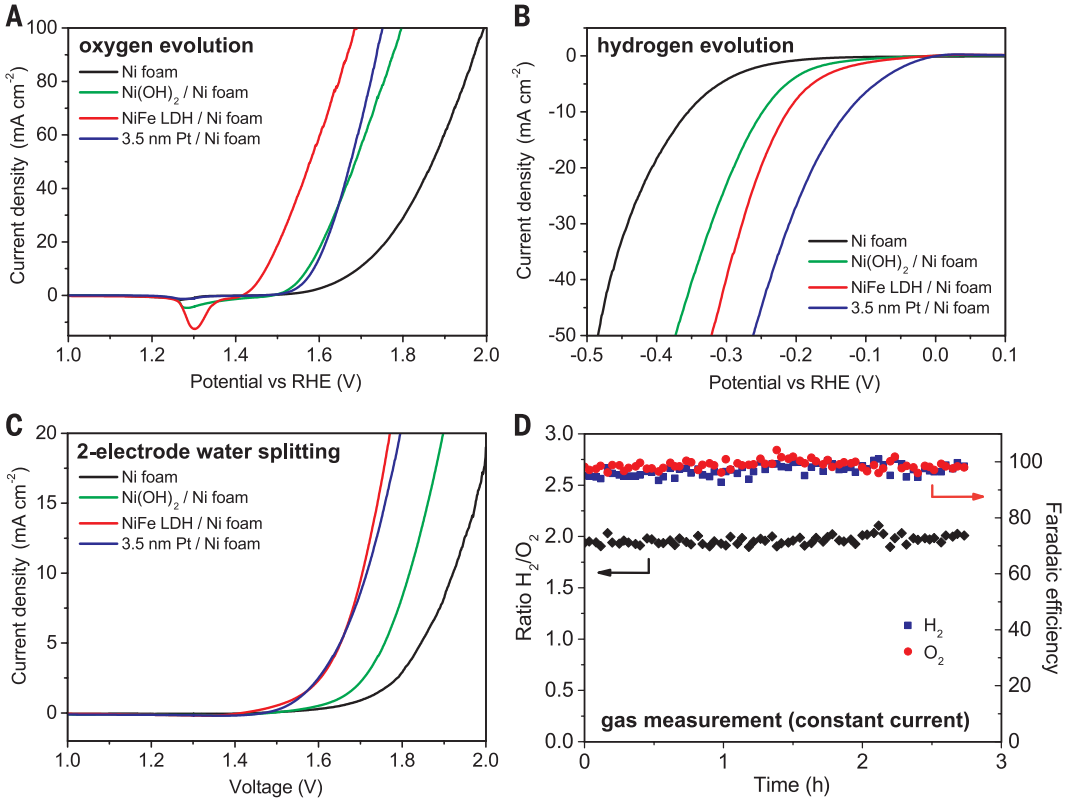

Fig. 2. Electrochemical performance of different catalyst electrodes by linear sweep voltammetry in 1 M NaOH aqueous electrolyte, and gas chromatography measurement of gases evolved from NiFe LDH electrodes. (**A**) OER characteristics of different catalyst electrodes in a three-electrode configuration, scanned in the direction from positive to negative potential on the RHE scale. (**B**) HER characteristics of different catalyst electrodes in a three-electrode configuration, scanned in the direction from negative to positive potential. (**C**) Overall water-splitting characteristics of different catalyst electrodes in a two-electrode configuration, scanned from 2.0 V to 1.0 V. All scan rates were 1 mV s^{-1}. (**D**) Gas ratio and Faradaic efficiency from gas chromatography measurement of evolved H_2 and O_2 from NiFe LDH/Ni foam electrodes in two-electrode configuration, driven by a galvanostat at a current density of 6 mA cm^{-2} (geometric).

are uncorrected and thus include resistive losses in the electrolyte). In the three-electrode configuration, the NiFe LDH/Ni foam electrode requires an overpotential (η_{OER}) of only 240 mV to reach a (projected geometric area) current density of 10 mA cm^{-2}. This potential is 100 mV less than the Pt/Ni foam electrode, whereas $Ni(OH)_2$/Ni foam electrode has nearly the same performance as the Pt/Ni foam for the OER. All of the modified electrodes show improved performance compared with pristine Ni foam. The small cathodic peak at 1.3 V versus RHE is due to the reduction of the oxidized NiFe LDH.

For the measurement of the catalytic activity toward the HER, the electrodes were swept at 1 mV s^{-1} from negative to positive potential on the RHE scale. The performance of the NiFe LDH/Ni foam electrode is much better than the bare Ni foam and slightly better than $Ni(OH)_2$/Ni foam, but worse than the Pt/Ni foam electrode (Fig. 2B). The NiFe LDH/Ni foam electrode requires an overpotential (η_{HER}) of 210 mV to achieve a current density of 10 mA cm^{-2}, which is 100 mV greater than the Pt/Ni foam electrode. The gains that we achieve on the practical level through the use of Earth-abundant catalysts offset the small loss in voltage that we observe. Considering that the HER activity in strong base is usually two to three orders lower than in acidic solution (*43*), the performance of this electrode is remarkable.

To go a step closer to the real application, overall water splitting in a two-electrode configuration was investigated (Fig. 2C). Overall, the NiFe LDH/Ni foam electrode shows nearly the same performance as the Pt/Ni foam electrode, with 10 mA cm^{-2} water-splitting current reached by applying just 1.7 V across the electrodes. To confirm the bifunctional activity of the NiFe LDH/Ni foam electrodes, the evolved gaseous products were quantified by means of gas chromatography. We confirmed quantitative Faradaic gas evolution at the predicted 2:1 ratio for hydrogen and oxygen, within experimental error (Fig. 2D). The exceptional bifunctionality, high activity, and low cost of the NiFe LDH/Ni foam electrode make it highly competitive for potential large-scale industrial applications.

The stability of the catalyst is very important because a practical water-splitting device should ideally last for several years (the longer the lifetime of the device, the lower the cost of the resulting hydrogen). To assess the stability of the NiFe LDH/Ni foam catalyst electrode, 1.8 V was applied to the electrodes, and there is a small degradation over a 10-hour test (fig. S1). However, the performance of the catalyst electrodes fully recovered in the second and third repeat experiments on the same electrode. Thus, although the mechanism of this decrease is yet unclear, the system benefits from the diurnal cycle, in which any slight reduction in photocurrent during daytime illumination is recovered at night. Further characterization of the catalyst electrodes can be found in figs. S2 to S4 and movie S1.

Using the above-demonstrated high-efficiency, low-cost perovskite solar cell and bifunctional water-splitting catalyst, an overall water-splitting cell was assembled (*28*). The schematic diagram of the device is shown in Fig. 3A. The perovskite solar cells were placed side by side and connected with wires to the immersed catalyst electrodes, and simulated solar irradiation provided the energy to split water. A generalized energy diagram is shown in Fig. 3B of the two perovskite solar cells connected in series as a tandem cell for water splitting. The tandem cell used in the integrated device exhibited the *J*–*V* response depicted in Fig. 3C, yielding a V_{OC} of 2.00 V while retaining a high PCE of 15.7%. The predicted operating current density of the combined system (normalized to the total illuminated area of the solar cells) is defined by the intersection of the *J*–*V* curves of both the perovskite tandem solar cell and the catalyst electrodes in the two-electrode configuration (Fig. 3C), giving a value of 10.0 mA cm^{-2}. This operating current, which corresponds to a solar-to-hydrogen efficiency of 12.3%, was confirmed with measurement in the standalone, unbiased light-driven configuration (Fig. 3D). To show the current more clearly, we present only the results of the initial 8 min in Fig. 3D. The performance of the device is further characterized under AM 1.5G chopped light illumination without applying any external bias for 2 hours (fig. S5). The fluctuation of the current under illumination is caused by bubble formation on the surface, which affects the effective surface area. The overall decrease in current on longer time scales is mainly due to the instability of the perovskite solar cell, a challenge that could be addressed by proper passivation and encapsulation techniques. A second representative device, featuring cells with greater stability but lower overall efficiency, is shown in fig. S6.

The operating point of the water-splitting cell occurs very close to the maximum power point of the perovskite tandem cell (9.61 mA cm^{-2} at 1.63 V) (Fig. 3C), indicating that minimal energy is lost in converting electrical to chemical energy in this system. In fact, we have achieved close to the maximum solar-to-hydrogen efficiency possible with the current state-of-the-art perovskite solar cell (in a side-by-side configuration). However, a solar-to-hydrogen efficiency up to 15% is reasonably possible with the fast development of perovskite solar cells (the theoretical upper limit for hydrogen generation in this configuration, as defined by a 1.5 eV band gap and the solar flux, is 17.8%). Improved stability of the device performance can be achieved through passivation of the perovskite solar cells. Furthermore, in the current study, the solar cells are wired with the Ni foam electrodes; however, alternative architectures are possible, for example, by directly attaching the water-splitting catalysts onto the back sides of the solar cells to form an integrated system.

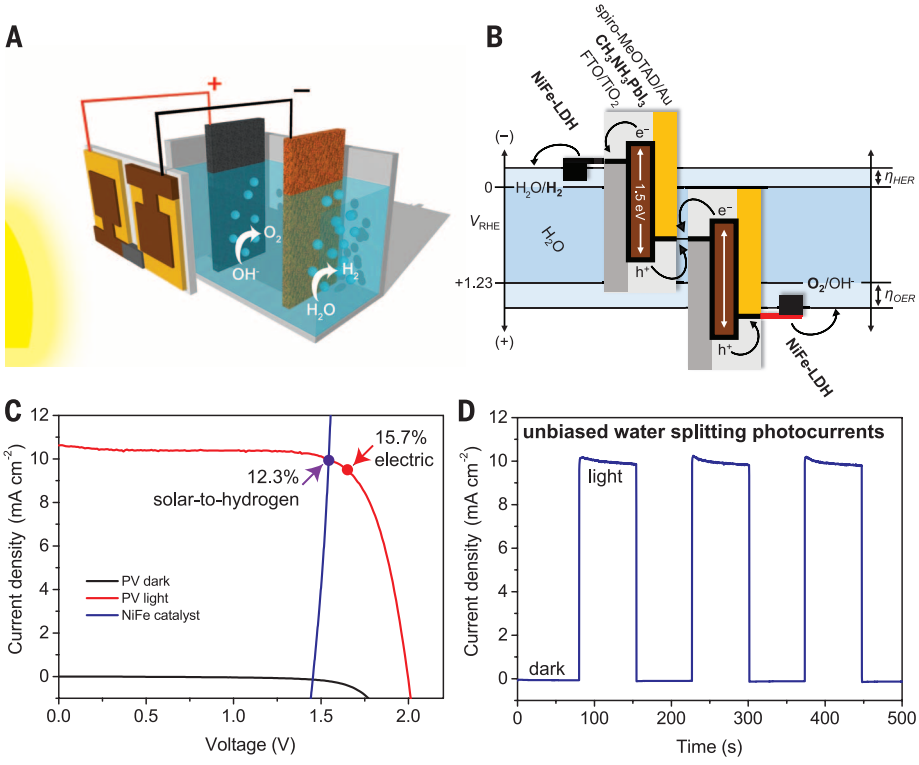

Fig. 3. Combination of the perovskite tandem cell with NiFe DLH/Ni foam electrodes for water splitting. (**A**) Schematic diagram of the water-splitting device. (**B**) A generalized energy schematic of the perovskite tandem cell for water splitting. (**C**) *J*–*V* curves of the perovskite tandem cell under dark and simulated AM 1.5G 100 mW cm^{-2} illumination, and the NiFe/Ni foam electrodes in a two-electrode configuration. The illuminated surface area of the perovskite cell was 0.318 cm^2, and the catalyst electrode areas (geometric) were ~5 cm^2 each. (**D**) Current density–time curve of the integrated water-splitting device without external bias under chopped simulated AM 1.5G 100 mW cm^{-2} illumination.

REFERENCES AND NOTES

1. B. O'Regan, M. Gratzel, *Nature* **353**, 737–740 (1991).
2. M. Grätzel, *Nature* **414**, 338–344 (2001).
3. A. Kojima, K. Teshima, Y. Shirai, T. Miyasaka, *J. Am. Chem. Soc.* **131**, 6050–6051 (2009).
4. J.-H. Im, C.-R. Lee, J.-W. Lee, S.-W. Park, N.-G. Park, *Nanoscale* **3**, 4088–4093 (2011).
5. H.-S. Kim *et al.*, *Sci. Rep.* **2**, 591 (2012).
6. M. M. Lee, J. Teuscher, T. Miyasaka, T. N. Murakami, H. J. Snaith, *Science* **338**, 643–647 (2012).
7. L. Etgar *et al.*, *J. Am. Chem. Soc.* **134**, 17396–17399 (2012).
8. J. Burschka *et al.*, *Nature* **499**, 316–319 (2013).
9. M. Liu, M. B. Johnston, H. J. Snaith, *Nature* **501**, 395–398 (2013).
10. J. H. Heo *et al.*, *Nat. Photonics* **7**, 486–491 (2013).
11. www.nrel.gov/ncpv/images/efficiency_chart.jpg.
12. A. J. Bard, M. A. Fox, *Acc. Chem. Res.* **28**, 141–145 (1995).
13. Y. Tachibana, L. Vayssieres, J. R. Durrant, *Nat. Photonics* **6**, 511–518 (2012).
14. M. G. Walter *et al.*, *Chem. Rev.* **110**, 6446–6473 (2010).
15. A. Fujishima, K. Honda, *Nature* **238**, 37–38 (1972).
16. O. Khaselev, J. A. Turner, *Science* **280**, 425–427 (1998).
17. M. W. Kanan, D. G. Nocera, *Science* **321**, 1072–1075 (2008).
18. S. Y. Reece *et al.*, *Science* **334**, 645–648 (2011).
19. J. Brillet *et al.*, *Nat. Photonics* **6**, 824–828 (2012).
20. J. Luo *et al.*, *Sci. Rep.* **2**, 451 (2012).
21. B. A. Pinaud *et al.*, *Energy Environ. Sci.* **6**, 1983–2002 (2013).
22. K. Zeng, D. Zhang, *Pror. Energy Combust. Sci.* **36**, 307–326 (2010).
23. R. E. Rocheleau, E. L. Miller, A. Misra, *Energy Fuels* **12**, 3–10 (1998).
24. T. J. Jacobsson, V. Fjallstrom, M. Sahlberg, M. Edoff, T. Edvinsson, *Energy Environ. Sci.* **6**, 3676–3683 (2013).
25. E. Edri, S. Kirmayer, M. Kulbak, G. Hodes, D. Cahen, *J. Phys. Chem. Lett.* **5**, 429–433 (2014).
26. E. Edri, S. Kirmayer, D. Cahen, G. Hodes, *J. Phys. Chem. Lett.* **4**, 897–902 (2013).
27. S. Ryu *et al.*, *Energy Environ. Sci.* **7**, 2614–2618 (2014).
28. Materials and methods are available as supplementary materials on *Science* Online.
29. J. Greeley, T. F. Jaramillo, J. Bonde, I. B. Chorkendorff, J. K. Nørskov, *Nat. Mater.* **5**, 909–913 (2006).
30. T. F. Jaramillo *et al.*, *Science* **317**, 100–102 (2007).
31. J. R. McKone, B. F. Sadtler, C. A. Werlang, N. S. Lewis, H. B. Gray, *ACS Catalysis* **3**, 166–169 (2012).
32. R. D. L. Smith *et al.*, *Science* **340**, 60–63 (2013).
33. F. Lin, S. W. Boettcher, *Nat. Mater.* **13**, 81–86 (2014).
34. T. W. Kim, K.-S. Choi, *Science* **343**, 990–994 (2014).
35. E. A. Hernández-Pagán *et al.*, *Energy Environ. Sci.* **5**, 7582–7589 (2012).
36. D. Merki, S. Fierro, H. Vrubel, X. Hu, *Chem. Sci.* **2**, 1262–1267 (2011).
37. M. Gao *et al.*, *J. Am. Chem. Soc.* **136**, 7077–7084 (2014).
38. X. Xia *et al.*, *Sci. Rep.* **2**, 981 (2012).
39. M. Gong *et al.*, *J. Am. Chem. Soc.* **135**, 8452–8455 (2013).
40. Z. Lu *et al.*, *Chem. Commun. (Camb.)* **50**, 6479–6482 (2014).
41. L. Trotochaud, S. L. Young, J. K. Ranney, S. W. Boettcher, *J. Am. Chem. Soc.* **136**, 6744–6753 (2014).
42. R. Subbaraman *et al.*, *Nat. Mater.* **11**, 550–557 (2012).
43. N. Danilovic *et al.*, *Angew. Chem. Int. Ed. Engl.* **51**, 12495–12498 (2012).

ACKNOWLEDGMENTS

The authors thank the Swiss Federal Office for Energy (PECHouse Competence Center, contract SI/500090–02), Nano-Tera NTF project TANDEM, the PECDEMO project, cofunded by Europe's Fuel Cell and Hydrogen Joint Undertaking under Grant Agreement 621252, the European Union for supporting the following projects: NANOMATCELL, under grant agreement 308997, MESO, and GLOBASOL, under the grant agreement 577490. In addition, we are grateful to the Swiss National Science Foundation and Swiss National Center of Competence in Research Molecular Ultrafast Science and Technology for financial support. M.G. thanks the European Research Council for financial support under the Advanced Research Grant (ARG 247404) "Mesolight" and acknowledges his affiliation as a visiting faculty member with Nanyang Technological University Singapore; the King Abdulaziz University Jeddah, Saudi Arabia; and the Advanced Institute for Nanotechnology at SKKU, Suwon, Korea. M.K.N. acknowledges his affiliation as a visiting faculty member to the King Abdulaziz University Jeddah, Saudi Arabia. H.J.F is thankful for the support from Singapore-Berkeley Research Initiative for Sustainable Energy (SinBeRISE) program. J.-H.I and N.-G.P are grateful to the National Research Foundation of Korea grants funded by the Ministry of Science, ICT & Future Planning (MSIP) of Korea under contracts NRF-2012M1A2A2671721 and NRF-2012M3A6A7054861 (Global Frontier R&D Program on Center for Multiscale Energy System).

SUPPLEMENTARY MATERIALS

www.sciencemag.org/content/345/6204/1593/suppl/DC1
Materials and Methods
Figs. S1 to S6
Reference (*44*)
Movies S1 and S2

3 July 2014; accepted 20 August 2014
10.1126/science.1258307

ATMOSPHERIC CHEMISTRY

Infrared-driven unimolecular reaction of CH_3CHOO Criegee intermediates to OH radical products

Fang Liu,[1] Joseph M. Beames,[1] Andrew S. Petit,[1] Anne B. McCoy,[2] Marsha I. Lester[1]*

Ozonolysis of alkenes, an important nonphotolytic source of hydroxyl (OH) radicals in the troposphere, proceeds through energized Criegee intermediates that undergo unimolecular decay to produce OH radicals. Here, we used infrared (IR) activation of cold CH_3CHOO Criegee intermediates to drive hydrogen transfer from the methyl group to the terminal oxygen, followed by dissociation to OH radicals. State-selective excitation of CH_3CHOO in the CH stretch overtone region combined with sensitive OH detection revealed the IR spectrum of CH_3CHOO, effective barrier height for the critical hydrogen transfer step, and rapid decay dynamics to OH products. Complementary theory provides insights on the IR overtone spectrum, as well as vibrational excitations, structural changes, and energy required to move from the minimum-energy configuration of CH_3CHOO to the transition state for the hydrogen transfer reaction.

Hydroxyl (OH) radicals, often termed the atmosphere's detergent, initiate the oxidative breakdown of most trace species in the lower atmosphere (*1*). Photolytic sources dominate the production of OH radicals in the daytime through solar photolysis of ozone, which generates $O(^1D)$ atoms that react with H_2O to form OH radicals, and nitrous acid, with sizable amounts of the latter being produced under high-NO_x conditions. The principal nonphotolytic source of atmospheric OH radicals is alkene ozonolysis, which is an important OH radical initiator in low-light conditions, urban environments, and heavily forested areas (*2*, *3*). Recent field campaigns indicate that alkene ozonolysis accounts for ~30% of tropospheric OH radicals in the daytime and essentially all of the smaller, yet appreciable, OH radical concentration at night (*4*, *5*).

Alkene ozonolysis occurs by cycloaddition of ozone across the C=C double bond and subsequent decomposition of the resultant primary ozonide, releasing ~50 kcal mol^{-1} of excess energy, to produce an energized carbonyl oxide species, known as the Criegee intermediate, and an aldehyde or ketone product (*6*). Further unimolecular decay of the Criegee intermediate leads to formation of OH radicals (*7*, *8*). The OH yield from ozonolysis changes substantially with alkene structure, increasing from ~10% for ethene via the simplest Criegee intermediate CH_2OO to more than 60% for ozonolysis of *trans*-2-butene (*9*, *10*), which proceeds through the methyl-substituted Criegee intermediate CH_3CHOO, the focus of the present study. (See table S1 for chemical structures of relevant species.) Concurrent detection of Criegee intermediates and OH products by photoionization mass spectrometry also shows a large increase in OH yield for alkyl-substituted Criegee intermediates compared to CH_2OO (*11*, *12*).

The efficient production of OH radicals upon ozonolysis of alkenes has been proposed to follow a 1,4-hydrogen atom shift mechanism for alkyl-substituted Criegee intermediates. The computed reaction coordinate, depicted in Fig. 1 for the more stable syn-conformer of CH_3CHOO, involves passage over a transition state with a five-membered, ringlike structure and migration of a hydrogen on the methyl group (an α-hydrogen) to the terminal oxygen to generate vinyl hydroperoxide (VHP, H_2C=CHOOH). This leads directly to O-O bond breakage, yielding OH radical and vinoxy products. A different mechanism is predicted for CH_2OO (and anticonformers of Criegee intermediates), with a substantially higher barrier to reaction that leads to dioxirane (*13*, *14*) and, based on kinetic studies, a much smaller yield of OH products under laboratory and atmospheric conditions (*9*).

This study focuses on infrared (IR) activation of cold Criegee intermediates to drive unimolecular decay to OH products. Specifically, we used IR excitation of *syn*-CH_3CHOO in the CH stretch overtone ($2\nu_{CH}$) region near 6000 cm^{-1} to surmount the barrier associated with 1,4-hydrogen transfer

[1]Department of Chemistry, University of Pennsylvania, Philadelphia, PA 19104-6323, USA. [2]Department of Chemistry and Biochemistry, The Ohio State University, Columbus, OH 43210-1173, USA.
*Corresponding author. E-mail: milester@sas.upenn.edu

Water photolysis at 12.3% efficiency via perovskite photovoltaics and Earth-abundant catalysts

Jingshan Luo *et al.*

Science **345**, 1593 (2014);
DOI: 10.1126/science.1258307